In 2nd EF Conference in Turbulent Heat Transfer, Vol. I, pp. 5.24–5.35,
Manchester, U.K., May 31 - June 5, 1998

COMPARISON OF SUBGRID-SCALE MODELS IN LES FOR TURBULENT CONVECTION FLOW WITH HEAT TRANSFER

Shia-Hui Peng* and Lars Davidson

Department of Thermo and Fluid Dynamics
Chalmers University of Technology
S-412 96 Gothenburg, Sweden

ABSTRACT

Dynamic subgrid-scale (SGS) modelling in LES for engineering flows usually uses Smagorinsky's eddy viscosity model as a basis, where the subgrid scaling is constructed by assuming a local equilibrium between the subgrid-scale turbulent shear production and dissipation rate. For turbulent thermal convection flows, an additional buoyant production term can also be included in this argument. The buoyant effect on the SGS eddy viscosity is then explicitly accommodated in the base model. This in turn forms the so-called *buoyancy SGS model*. With this model, a problem usually encountered when solving thermal convection flows is that non-real solutions may arise. To remedy this problem, a new SGS time scaling is proposed to re-construct the buoyancy eddy viscosity base model. In the modified model, the magnitude of the strain rate tensor is employed to weight the SGS time scaling in the base model including buoyancy effects. For thermally stratified flows, this approach also makes the base model be capable of accounting for some energy backscatter from subgrid scales to resolved large scales. The modified model was applied to a Rayleigh-Bénard convection flow, and compared with the scalar model and the buoyancy model. The results are found to be in good agreement with both DNS and experimental data.

1 INTRODUCTION

Computation of turbulent flows is complicated owing to the large range of scales that exists in these flows. Traditional Reynolds-averaging approaches (RANS), e.g., the two-equation models and the second-moment models, are not always satisfactory because the physics of the various scales that contribute to the correlation terms is different. On the other hand, direct numerical simulations (DNS) can as yet not handle high Reynolds-number turbulent flows owing to the limitation in computer capacity. In the past two decades, large eddy simulation (LES) has gained extensive attention for its higher physical ability to describe turbulence than RANS and lower computational cost than DNS.

The basic philosophy of LES is to explicitly resolve the large-scale motion and to model the small scales. To distinguish the small-scale eddies from resolved large scales, a spatial filtering process is usually applied to the Navier-Stokes equations. The resultant subgrid-scale stress tensor, which contains the information about the effect of smaller scales on the evolution of the larger scales, is presumed to be more universal in nature than the Reynolds-averaging stress tensor and thus more amenable to successful modelling. The SGS stresses can be modelled at different levels of complexity. The most widely used SGS model is the Smagorinsky model (1), where the SGS stress tensor is modelled in alignment with the local large-scale strain rate tensor through the eddy viscosity concept. After Smagorinsky's initial development, a number of SGS models has been proposed, examples of which are the vorticity model by Ferziger (2), the scale-similarity and mixed models by Bardina *et al.* (3) and the SGS model based on renormalization group theory by Yakhot *et al.* (4).

The existing conventional SGS model has been successfully applied to the LES of transitional and turbulent flows. Problems have also arisen in these applications, however. The most serious one is the *ad hoc* model constant, which varies within a large range for different flow problems. Other limitations of the Smagorinsky model and of its variants were pointed out in some recent articles, e.g., by Moin *et al.* (5). The dynamic SGS eddy viscosity model developed by Germano *et al.* (6, 7) overcomes most of the deficiencies in the Smagorinsky model. The dynamic approach allows the model coefficient to be a function of both space and time by extrapolating information from the smallest, resolved large-scale structure. In contrast to the absolutely dissipative behavior with the Smagorinsky model, dynamic models are able to render negative SGS eddy coefficient to account for energy backscatter from subgrid scales to resolved large scales, which has been shown to be an effective function in LES, particularly for transitional flows (8).

Effort has also been made in recent years to apply the dynamic SGS model to turbulent thermal convection flows. Using four different SGS eddy viscosity/diffusivity base models, Cabot (9) performed

*Also Department of Work Organization and Technology, National Institute for Working Life, S-171 84 Solna, Sweden.

LES for Rayleigh-Bénard convection flows and flows in an internally heated channel. It was found that, as compared with the buoyancy model for which the SGS Prandtl number, Pr_t, is iteratively determined, the Eidson model (10) promises better predictions and less computational effort by simply setting Pr_t as a constant. Wong and Lilly (11) compared two dynamic SGS models, i.e. the stratification formulation and the scaling formulation for the Rayleigh-Bénard convection at $Ra = 3.8 \times 10^5$. The stratification formulation includes a buoyancy term as in the Eidson model (10), but the SGS turbulent Prandtl number is dynamically computed. This model is thus the same as the buoyancy model in Ref. (9). Wong and Lilly also reported that the stratification formulation (i.e. the buoyancy model) is computationally inefficient due to iterative determination for Pr_t and that this formulation occasionally gives non-real solutions, as shown by Cabot (9). Recently, Bergstrom and Huang (12) applied a dynamic SGS model based on the scalar model (with no buoyancy-related term in the eddy viscosity/diffusivity formulation) to a buoyant cavity flow. A rather limited success in the prediction was reported. Other applications and developments of LES for handling turbulent buoyant flows have been made, e.g., by Wang and Pletcher (13) and Canuto *et al.* (14).

In our work on LES for buoyancy-driven convection flows, it has also been found that the buoyancy model, as used in Refs (9) and (11), sometimes induces non-real solutions. This problem may break down the computation unless some measures are taken, for example, by setting a zero SGS eddy viscosity as the SGS buoyancy production is negatively dominant over the SGS shear production. However, this approach may be inappropriate since a negative SGS eddy viscosity is thought to be physically reasonable in terms of accounting for energy backscatter that often occurs in non-laminar flow regions. In addition, the dynamic procedure might be preserved better without directly and artificially tuning the SGS eddy viscosity, which, instead, should be quantified by both the model coefficient and the SGS turbulent scaling. Peng and Davidson (15) recently proposed a new time scaling to re-construct the SGS buoyancy model in combination with the Smagorinsky model. This approach is able to overcome the problem of entailing non-real solutions in cases of existing stable and significant thermal stratification. In this work, the Smagorinsky model, the Eidson buoyancy model and the modified buoyancy model are applied to a turbulent Rayleigh-Bénard convection flow and compared with each other as well as with DNS and laboratory data.

2 THE SGS CLOSURE FORMULATION

In Large eddy simulation, a filter function is used to split the span of turbulence scales somewhere in the Kolmogorov equilibrium region. The filtered large scales are resolved. The subgrid-scale turbulence is assumed to be more isotropic in nature and is modelled by using the information from the smallest resolved large-scale eddies, requiring less adjustments than RANS approach. Applying the filtering process to the Navier-Stokes equations gives rise of an SGS stress tensor, which represents the energy occurrence between filtered large scales and subgrid scales. The modelling of these unknown SGS stresses has mostly been based on the eddy viscosity concept as in RANS approach. Similar to the Reynolds stresses resulted from the time-averaging process in RANS, the anisotropic part of the SGS stress tensor is modelled in alignment with the local strain rate tensor, i.e.,

$$\tau_{ij} - \frac{\delta_{ij}}{3}\tau_{kk} = -2\nu_t \bar{S}_{ij}, \tag{1}$$

where ν_t is the SGS eddy viscosity and $\bar{S}_{ij}$ is the large-scale strain rate tensor, reading

$$\bar{S}_{ij} = \frac{1}{2}\left(\frac{\partial \bar{u}_i}{\partial x_j} + \frac{\partial \bar{u}_j}{\partial x_i}\right). \tag{2}$$

In analogy to τ_{ij}, the resultant SGS heat fluxes in the filtered energy equation are modelled as

$$h_j = -\alpha_t \frac{\partial \bar{\theta}}{\partial x_j}, \tag{3}$$

where α_t is the SGS eddy diffusivity.

By assuming that the subgrid scales are in local equilibrium, for which a balance holds between the SGS turbulent production and turbulent dissipation rate, the SGS eddy viscosity, ν_t, can be derived as $\nu_t = C\Delta^2/\mathcal{T}$. Similarly, the SGS eddy diffusivity, α_t, is expressed as $\alpha_t = C_t\Delta^2/\mathcal{T}$. In the so-called dynamic *scalar model*, the time scaling, $\mathcal{T}_S$, is equal to the reciprocal of the magnitude of the local strain rate tensor, i.e. $\mathcal{T}_S = 1/|\bar{S}|$, and $|\bar{S}| = \sqrt{2\bar{S}_{ij}\bar{S}_{ij}}$, see e.g. Refs (16, 17). The SGS Prandtl number is given by $Pr_t = \nu_t/\alpha_t = C/C_t$.

Eidson (10) derived the SGS eddy viscosity with a buoyancy term included in the SGS turbulent production. This brings about the *buoyancy model* in which the SGS eddy viscosity takes the form of

$$\nu_t = C\Delta^2\left(|\bar{S}|^2 + \frac{\beta}{Pr_t}\frac{\partial \bar{\theta}}{\partial x_j}g_k\delta_{kj}\right)^{\frac{1}{2}}. \tag{4}$$

Similarly, the SGS eddy diffusivity in Eidson's buoyancy model is expressed as

$$\alpha_t = C_t\Delta^2\left(|\bar{S}|^2 + \frac{\beta}{Pr_t}\frac{\partial \bar{\theta}}{\partial x_j}g_k\delta_{kj}\right)^{\frac{1}{2}}. \tag{5}$$

In equations (4) and (5), g_k denotes the gravitational vector, $g_k = (0, -g, 0)$. The $1/\mathcal{T}_B$ scaling that appears in the buoyancy model is then

$$\frac{1}{\mathcal{T}_B} = \left(|\bar{S}|^2 - \frac{g\beta}{Pr_t}\frac{\partial \theta}{\partial x_j}\delta_{2j}\right)^{\frac{1}{2}}. \tag{6}$$

With this $1/\mathcal{T}_B$ scaling, the eddy viscosity has to be constrained to be equal to zero as $\mid \bar{S} \mid^2 < \frac{g\beta}{Pr_t}\frac{\partial\theta}{\partial x_j}\delta_{2j}$ to avoid entailing non-real solutions. Winckelmans *et al.* (18) evaluated several base models with different choices for the $1/\mathcal{T}$ scaling in an *a priori* test of SGS models using available DNS data. It was found that the choice of $1/\mathcal{T}$ scaling in the eddy viscosity is unimportant as it does not significantly affect the correlations between modelled and exact SGS quantities. This suggests that the $1/\mathcal{T}$ scaling does not necessarily need to be derived from the production-dissipation equilibrium argument. Moreover, the problem of inducing non-real solutions with the buoyancy base model, i.e. equation (6), needs to be eliminated. Therefore, the new $1/\mathcal{T}_N$ scaling is proposed as

$$\frac{1}{\mathcal{T}_N} \equiv \bar{N} = \frac{1}{\mid \bar{S} \mid}\left(\mid \bar{S} \mid^2 - \frac{g\beta}{Pr_t}\frac{\partial\theta}{\partial x_j}\delta_{2j}\right). \qquad (7)$$

The eddy viscosity and the eddy diffusivity in the modified buoyancy base model are then expressed, respectively, as

$$\begin{aligned} \nu_t &= C\Delta^2\bar{N} \\ &= C\Delta^2\frac{1}{\mid \bar{S} \mid}\left(\mid \bar{S} \mid^2 - \frac{g\beta}{Pr_t}\frac{\partial\bar{\theta}}{\partial x_j}\delta_{2j}\right) \end{aligned} \qquad (8)$$

and

$$\begin{aligned} \alpha_t &= C_t\Delta^2\bar{N} \\ &= C_t\Delta^2\frac{1}{\mid \bar{S} \mid}\left(\mid \bar{S} \mid^2 - \frac{g\beta}{Pr_t}\frac{\partial\bar{\theta}}{\partial x_j}\delta_{2j}\right). \end{aligned} \qquad (9)$$

Note that for isothermal flows, $\frac{\partial\bar{\theta}}{\partial x_j}\delta_{2j} \equiv 0$, this model then turns out to be the conventional Smagorinsky model, i.e. the scalar model. It is interesting to note a relation for the SGS time scales with the above three base models, i.e. $\mathcal{T}_N/\mathcal{T}_B = \mathcal{T}_B/\mathcal{T}_S$. The modified model is thus a combination of the Smagorinsky model and Eidson's buoyancy model. This combination suggests that the SGS time scale given by the buoyancy model nestles between those given by the scalar model and by the modified model. For flows with stable thermal stratification, the modified model is expected to produce the largest time scale, and the smallest for flows with unstable thermal stratification.

Introducing equations (8) and (9) into the dynamic procedure developed by Germano *et al.* (6) and modified later by Lilly (19), the model coefficients C, C_t and Pr_t can be dynamically determined. The dynamic SGS modelling is based on the use of two filters. A test filter (denoted by a curved overbar) is employed in addition to the grid filter (denoted by an overbar). The grid filter is used to define the subgrid scales, while the test filter, whose width is larger than the grid filter width, produces information from the smallest resolved large-scale structure to formulate the SGS stresses and heat fluxes. Furthermore, a mathematical identity is exploited to determine the model coefficients. This identity relates the SGS stresses on the grid-filtering level, τ_{ij}, and on the test-filtering level, T_{ij}, (and thus similarly the heat fluxes, h_j and H_j, on these two filtering levels) to the resolvable residual stresses, $\mathcal{L}_{ij}$ (and thus similarly the resolvable residual heat fluxes, $\mathcal{E}_j$).

As proposed by Germano *et al.* (6), the test filter width, $\widehat{\Delta}$, is chosen to be twice the grid filter width, Δ, i.e. $\widehat{\Delta} = 2\Delta$. In analogy to the SGS stress tensor in equation (1), the stress tensor on the test filtering level is expressed as

$$T_{ij} - \frac{\delta_{ij}}{3}T_{kk} = -2\widehat{\nu_t}\,\widehat{\bar{S}}_{ij}. \qquad (10)$$

Similarly, the heat fluxes, H_j, are

$$H_j = -\widehat{\alpha_t}\frac{\partial\,\widehat{\bar{\theta}}}{\partial x_j}. \qquad (11)$$

The eddy viscosity and diffusivity for the modified model (and similarly for the scalar model and the buoyancy model), on the test level are expressed, respectively, as

$$\begin{aligned} \widehat{\nu_t} &= C\widehat{\Delta}^2\widehat{\bar{N}} \\ &= C\widehat{\Delta}^2\overline{\frac{1}{\mid \bar{S} \mid}\left(\mid \bar{S} \mid^2 - \frac{g\beta}{Pr_t}\frac{\partial\bar{\theta}}{\partial x_j}\delta_{2j}\right)} \end{aligned} \qquad (12)$$

and

$$\begin{aligned} \widehat{\alpha_t} &= C_t\widehat{\Delta}^2\widehat{\bar{N}} \\ &= C_t\widehat{\Delta}^2\overline{\frac{1}{\mid \bar{S} \mid}\left(\mid \bar{S} \mid^2 - \frac{g\beta}{Pr_t}\frac{\partial\bar{\theta}}{\partial x_j}\delta_{2j}\right)}. \end{aligned} \qquad (13)$$

In deriving equations (12) and (13), a scale-invariance assumption has been made. It is assumed that C and C_t are very slowly varying functions of space. This assumption thus allows to use the same model coefficients at both the grid and test filtering levels. The Germano identity (6) indicates that

$$\mathcal{L}_{ij} = T_{ij} - \widehat{\tau}_{ij} = \overline{\bar{u}_i\bar{u}_j} - \widehat{\bar{u}}_i\widehat{\bar{u}}_j. \qquad (14)$$

For the heat fluxes, this identity takes the following form

$$\mathcal{E}_j = H_j - \widehat{h}_j = \overline{\bar{u}_j\bar{\theta}} - \widehat{\bar{u}}_j\widehat{\bar{\theta}}. \qquad (15)$$

The right-hand-side residual stresses and fluxes in equations (14) and (15) are resolvable quantities. This feature is then employed to compute the model coefficients. Introducing the SGS eddy viscosity/diffusivity models into the above identities yields

$$\begin{aligned} \mathcal{L}_{ij} - \frac{\delta_{ij}}{3}\mathcal{L}_{kk} &= -2C\widehat{\Delta}^2\widehat{\bar{N}}\,\widehat{\bar{S}}_{ij} \\ &\quad +2C\Delta^2\overline{\bar{N}\bar{S}_{ij}} \end{aligned} \qquad (16)$$

and

$$\mathcal{E}_j = -C_t \widehat{\Delta}^2 \widehat{\bar{N}} \frac{\partial \widehat{\bar{\theta}}}{\partial x_j} + C_t \Delta^2 \widehat{\bar{N} \frac{\partial \bar{\theta}}{\partial x_j}}. \quad (17)$$

By means of the least square approach proposed in Ref. (19), the model coefficients, C and C_t, are formulated, respectively, as

$$\begin{aligned} C &= -\frac{\mathcal{L}_{ij} M_{ij}}{2 M_{ij} M_{ij}}; \\ M_{ij} &= \widehat{\Delta}^2 \widehat{\bar{N}} \widehat{\bar{S}}_{ij} - \Delta^2 \widehat{\bar{N} \bar{S}_{ij}} \end{aligned} \quad (18)$$

and

$$\begin{aligned} C_t &= -\frac{\mathcal{E}_j Q_j}{Q_j Q_j}; \\ Q_j &= \widehat{\Delta}^2 \widehat{\bar{N}} \frac{\partial \widehat{\bar{\theta}}}{\partial x_j} - \Delta^2 \widehat{\bar{N} \frac{\partial \bar{\theta}}{\partial x_j}}. \end{aligned} \quad (19)$$

When using equations (18) and (19) to compute the model coefficients, two principal deficiencies exist: the scale-invariance assumption for the model coefficient is not mathematically self-consistent since it wipes out the time- and spatially-dependent feature from a filtering operation; second, the model is ill-conditioned because the denominators in equations (18) and (19) can be very small, which in turn causes numerical instability. The first can be partly overcome by using approximately localized model coefficients as in, e.g Ref. (20). To remedy the second problem, as in Germano *et al.* (6), the model coefficients are assumed to be only functions of time and inhomogeneous directions. For the Rayleigh-Bénard flow considered in this work, for example, a spatial-averaging for the numerators and denominators in (18) and (19) is then made over two directions of flow homogeneity (the $x-$ and $z-$directions), denoted by $< \cdot >_{xz}$. The model coefficients are thus functions of time and of only the direction normal to the walls, i.e.

$$C(t,y) = -\frac{< \mathcal{L}_{ij} M_{ij} >_{xz}}{2 < M_{ij} M_{ij} >_{xz}}, \quad (20)$$

and

$$C_t(t,y) = -\frac{< \mathcal{E}_j Q_j >_{xz}}{< Q_j Q_j >_{xz}}. \quad (21)$$

Furthermore, to remove the numerical instability attributed to negative total viscosity arising at some points in the flow domain, the total viscosity at those points is artificially set to zero. Nonetheless, this clipping approach allows a small amount of energy backscatter.

There is another model coefficient, Pr_t, in the modified model and the buoyancy model that must be determined. This can be accounted for by using an iterative scheme as in Refs (11, 12) with respect to equations (20) and (21) to get $Pr_t = C/C_t$. Applying such a scheme to the buoyancy model, i.e. equations (4) and (5), Cabot (9) pointed out that an iterative determination of Pr_t doubled the cost on computing the SGS model and sometimes gave either non-real or multiple solutions. It was found in Ref. (9) that, in comparison with the scalar model, the buoyancy model entailed little difference in the results, as Pr_t was locally computed. Instead, improved simulations were obtained by simply using a constant Pr_t in the buoyancy base model with $Pr_t = 0.4$ as used in Ref. (10). This approach, moreover, requires less computational effort, see Ref. (9).

In this work, the scalar model has also been used for comparison. Comparing to the buoyancy model or the modified model, the scalar model is equivalent to setting $Pr_t = \infty$, see equations (4) and (5) or equations (8) and (9). Because of the too costly computation, instead of using an iterative scheme (e.g. Newton's method), we have used the value of C/C_t at the previous time step, say, $(n-1)$, to approximate Pr_t at time step n, giving

$${Pr_t}^n \simeq \left(\frac{C}{C_t}\right)^{n-1}. \quad (22)$$

Equation (22) is an approximation similar to Piomelli and Liu's proposal (20), where they computed the model coefficient, C, in their localized dynamic model by employing the "zeroth-order approximation" and the "first-order approximation". It was argued that the model coefficient is fairly slowly-varying function of time because of the temporal filtering introduced implicitly by the spatial filtering. In addition to using equation (22), $Pr_t = 0.4$ has also been employed for comparison when using both the modified model and the buoyancy model.

3 NUMERICAL METHOD

The central differencing finite-volume method was used to discretize the differential governing equations on a collocated grid, and the second-order Crank-Nicholson scheme was employed for temporal discretization (22, 23).

The filtered Navier-Stokes equation for $\bar{u}_i$ can be written as

$$\begin{aligned} &\frac{\partial \bar{u}_i}{\partial t} + \frac{\partial}{\partial x_j}\left(\bar{u}_i \bar{u}_j\right) \\ &= -\frac{1}{\rho}\frac{\partial \bar{p}}{\partial x_i} + \nu \frac{\partial^2 \bar{u}_i}{\partial x_j \partial x_j} - \frac{\partial \tau_{ij}}{\partial x_j}. \end{aligned} \quad (23)$$

By means of an implicit, two-step time advancement method, this equation is discretized as the following

$$\begin{aligned} &\bar{u}_i^{n+1} = \bar{u}_i^n + \Delta t H\left(\bar{u}_i^n, \bar{u}_i^{n+1}\right) \\ &-\frac{1}{\rho}\alpha \Delta t \frac{\partial \bar{p}^{n+1}}{\partial x_i} - \frac{1}{\rho}(1-\alpha)\Delta t \frac{\partial \bar{p}^n}{\partial x_i}, \end{aligned} \quad (24)$$

where $H\left(\bar{u}_i^n, \bar{u}^{n+1}\right)$ denotes the discrete terms on the right-hand side of equation (23) except the pressure-gradient term. Equation (24) is first solved for $\bar{u}_i^{n+1}$.

To reinforce the coupling between the velocity and pressure fields, an intermediate velocity field is then computed as

$$\bar{u}_i^* = \bar{u}_i^{n+1} + \frac{1}{\rho}\alpha\Delta t\frac{\partial \bar{p}^{n+1}}{\partial x_i}. \quad (25)$$

Taking the divergence of equation (25) leads to a Poisson equation for the pressure, i.e.

$$\frac{\partial^2 \bar{p}^{n+1}}{\partial x_i \partial x_i} = \frac{\rho}{\alpha\Delta t}\frac{\partial \bar{u}_i^*}{\partial x_i}. \quad (26)$$

Note that the continuity condition has been implicitly applied at time step $(n+1)$ in the diverging procedure from equation (25) to equation (26). The Poisson equation is solved with an efficient multigrid method (24). The resultant pressure, together with the intermediate velocity obtained through equation (25), is then used to correct the velocity at the volume faces, which consequently gives a continuity-satisfied velocity field.

The box filter was used in the filtering procedure. In a finite volume calculation, the test-filtered flow quantities can be computed by volume-averaging the grid-scale filtered variables over test cells by assuming linear variation of these variables, see Ref. (25). A detailed description of the solution procedure can be found in Refs (22, 26).

4 RESULTS AND DISCUSSION

In this section, the above three SGS models, i.e. the scalar model, the buoyancy model and the modified model, are applied to the Rayleigh-Bénard convection at a Rayleigh number of $Ra = 3.8 \times 10^5$ and a molecular Prandtl number of $Pr = 1.0$. Available DNS and experimental data are used for comparison.

The Rayleigh-Bénard convection is induced in a horizontal channel by a heated bottom boundary and a cooled top boundary. The computational domain used is $6 \times 1 \times 6$, with a grid resolution of $48 \times 48 \times 48$. The boundary condition for the pressure is the Neumann condition at the top and bottom wall surfaces. Periodical boundary conditions have been employed for all variables in the longitudinal and spanwise directions ($x-$ and $z-$directions). The no-slip condition is used at the walls for the velocity components, $\bar{u}_i$. Constant temperatures are specified at the horizontal wall surfaces, with a temperature difference of $\Delta\theta = 10^oC$. The computation started with a result computed using the Smagorinsky model. The time unit in the Rayleigh-Bénard convection is $t_0 = D/u_0$, where D is the height of the fluid layer, $u_0 = \sqrt{g\beta\Delta\theta D}$, and β is the volumetric expansion coefficient. The time interval is about $0.05t_0$. The number of time steps used in each calculation is generally 60000. This corresponds to approximately $3000t_0$. The data are analyzed over a period of about $800t_0$. The time-averaged quantity is thus obtained through $< \phi >_t = \int_{T_0}^{T_1} \phi(t')dt'/(T_1 - T_0)$, with $T_0 \simeq 2200t_0$ and $T_1 \simeq 3000t_0$. The time-averaging process is denoted here by $< \cdot >_t$. For convenience, however, this notation will be dropped for time-averaged model coefficients in the following discussion.

Figure 1 shows the history of time-averaging the model coefficients at the mid-point of the domain, where the modified SGS model was used with Pr_t computed by equation (22). It is shown that all the model coefficients at this point remain nearly unchanged with increasing averaging time after $t \simeq 200t_0$. This demonstrates that the time period used for time-averaging in this work is sufficient for data analyses.

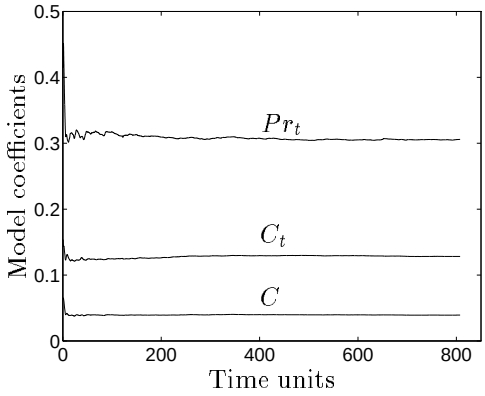

Figure 1: History of time-averaging model coefficients at the mid-point of the domain using the modified model with Pr_t computed by Eq. (22).

In Fig. 2, the vertical distributions of the time-averaged model coefficients are compared when using various SGS models. A large variation can be observed between different models. With the modified model, the coefficients appear to be rather sensitive to the specification of Pr_t: they are generally larger in the core region and smaller in the near-wall outer region when $Pr_t = 0.4$ is used than when Pr_t is locally computed with equation (22). Using the buoyancy model and computing Pr_t with equation (22), non-real solutions were detected occasionally in computations for C and C_t in the near-wall region, which have been smoothed in the figure by means of cut-off. Near the wall, the viscous effect is dominant, where C and C_t are rather small and even become slightly negative indicating a small amount of energy backscatter. In the core region of the flow domain, the scalar model gives a rather flat distribution for C with a value of about 0.048, and the modified model produces a nearly constant distribution for C_t. The buoyancy model calculates a C-profile between those determined with the scalar model and the modified model. Moreover, this model produces very similar distributions for C and C_t when using either of the above two specifications for Pr_t except in the core region, where the coefficients are slightly smaller as

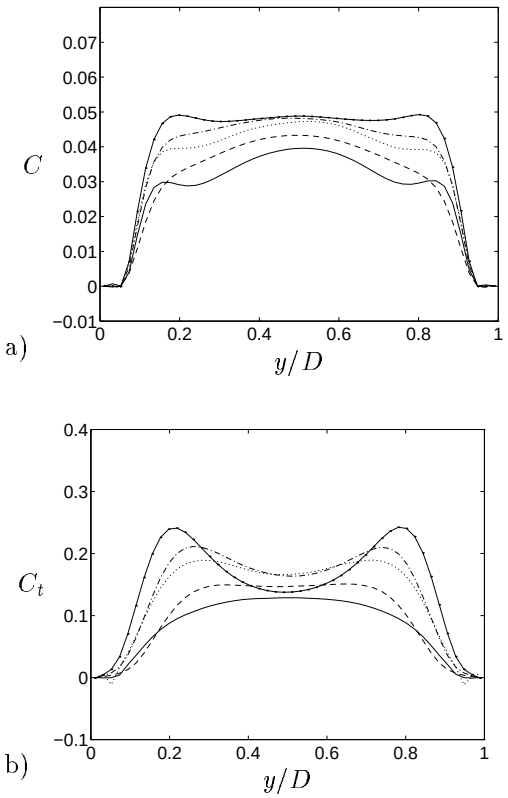

Figure 2: Vertical distributions of computed model coefficients: a) Model coefficient C; b) Model coefficient C_t. Solid-dotted line: Scalar model; Dash-dotted line: Buoyancy model ($Pr_t = 0.4$); Dotted line: Buoyancy model (Pr_t computed with Eq. (22)); Dashed line: Modified model ($Pr_t = 0.4$); Solid line: Modified model (Pr_t computed with Eq. (22)).

Pr_t is locally computed with equation (22).

In Fig. 3, the SGS Pr_t computed with different models is compared. Since Pr_t is not dynamically calculated in the scalar model, it is obtained by taking $Pr_t = C/C_t$ in this figure, and the same is done for both the buoyancy and the modified models as $Pr_t = 0.4$ is used. None of the three models reproduces the standard constant SGS Prandtl number ($Pr_t = 0.4$) as proposed by Eidson (10). The scalar model gives a value of about 0.39 for Pr_t in a narrow core region between $y/D \simeq 0.47 \sim 0.53$, while a value of about 0.3 is given in a wider region by the modified model. Near the walls, the SGS Prandtl number computed by the modified model becomes much larger, reaching 0.68 as equation (22) is used and 0.84 with $Pr_t = 0.4$. Using the buoyancy model, Cabot (9) showed a similar distribution tendency for Pr_t in an LES for Rayleigh-Bénard convection at $Ra = 1 \times 10^7$ and $Pr = 0.71$. A large variation occurs mainly in the near-wall region. Due to slightly negative values for C or C_t close to the wall, Pr_t also becomes negative there. However, the negative Pr_t hardly influences the simulation of the convective flow variables, because both C and C_t are so small in this near-wall viscous boundary layer that the computed SGS eddy coefficients, ν_t and α_t, are much smaller than their molecular counterparts.

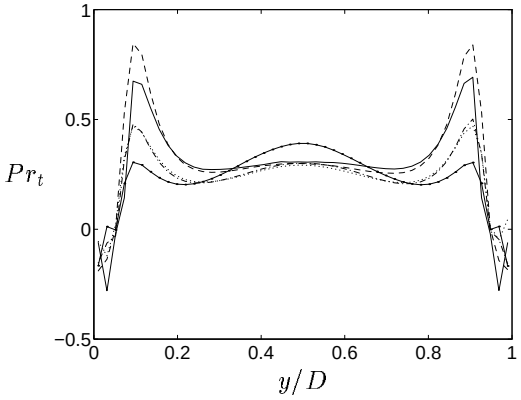

Figure 3: Vertical distributions of computed SGS Pr_t (same legend as in Fig. 2).

The computed vertical distributions for the root mean squares of velocity components and temperature, $\sqrt{< (\bar{u}_i - < \bar{u}_i >_t)^2 >_{txz}}$ and $\sqrt{< (\bar{\theta} - < \bar{\theta} >_t)^2 >_{txz}}$, i.e. $\bar{u}_{rms}$ or $\bar{w}_{rms}$, $\bar{v}_{rms}$ and $\bar{\theta}_{rms}$ are shown in Fig. 4. Also shown in this figure is the vertical profile of the dimensionless temperature, $(< \bar{\theta} >_{txz} - \bar{\theta}_{cw})/\Delta\theta$, where $\bar{\theta}_{cw}$ is the temperature of the cooled top wall surface. The buoyancy model produces very similar simulations regardless of whether Pr_t is set as a constant ($Pr_t = 0.4$) or locally determined with equation (22) except in the near-wall region where using $Pr_t = 0.4$ gives slightly better distributions. In the following comparisons, the distributions computed by the buoyancy model together with equation (22) are not included, unless otherwise stated. All the models give similar and reasonable results in comparison with both the DNS data from Refs (27, 28) and the laboratory data from Ref. (29). The $\bar{w}_{rms}$ profile (not shown here) is nearly identical to the $\bar{u}_{rms}$ profile. In Fig. 4, the experimental data are adopted from Deardorff and Willis' laboratory investigation (29) for $Ra = 6.3 \times 10^5$. All the models under-predict $\bar{v}_{rms}$ in the core region of the flow domain as compared with the measured and DNS data, but gives better predictions than those in Ref. (11) for the same flow problem, where the buoyancy model (termed *stratification formulation* in Ref. (11)) was applied. The comparison with the experimental data shows that the $\bar{\theta}_{rms}$ profile is generally over-predicted by all the models. Eidson (10) showed a similar prediction in a previous LES. The results, however, agree better with the DNS data for $Pr = 0.71$ given by Wörner and Grötzbach (28). In the DNS by Moeng and Rotunno (27), with $Pr_t = 1.0$, it was stated that the root-mean-square of the temperature has a maxima of 0.15 located about 0.07 away from both walls and a value of about 0.08 at mid-level. This has been approximately reflected in the present prediction as

shown in Fig. 4 c).

In spite of the fact that the model coefficients vary with different models, only can very small difference be observed in the predictions given in Fig. 4. This seems to indicate that the large-scale statistics are fairly insensitive to the base model used for the flow considered. In the LES of Rayleigh-Bénard convection at $Ra = 1 \times 10^7$, Cabot (9) also showed that the scalar model and the buoyancy model gave very similar results. He attributed this to several possible factors: the buoyancy term is generally less than, or comparable to the strain term, or, even with a different scaling, the dynamic eddy viscosities/diffusivities tend to self-adjust to a similar level. To gain a quantitative understanding, the strain term, $\mid \bar{S} \mid^2$, is compared with the buoyancy-related term, $\frac{g\beta}{Pr_t}\frac{\partial \bar{\theta}}{\partial y}$, in the expression for SGS eddy coefficients. This is shown in Fig. 5, where the modified model is employed using $Pr_t = 0.4$. It can be seen that the buoyancy

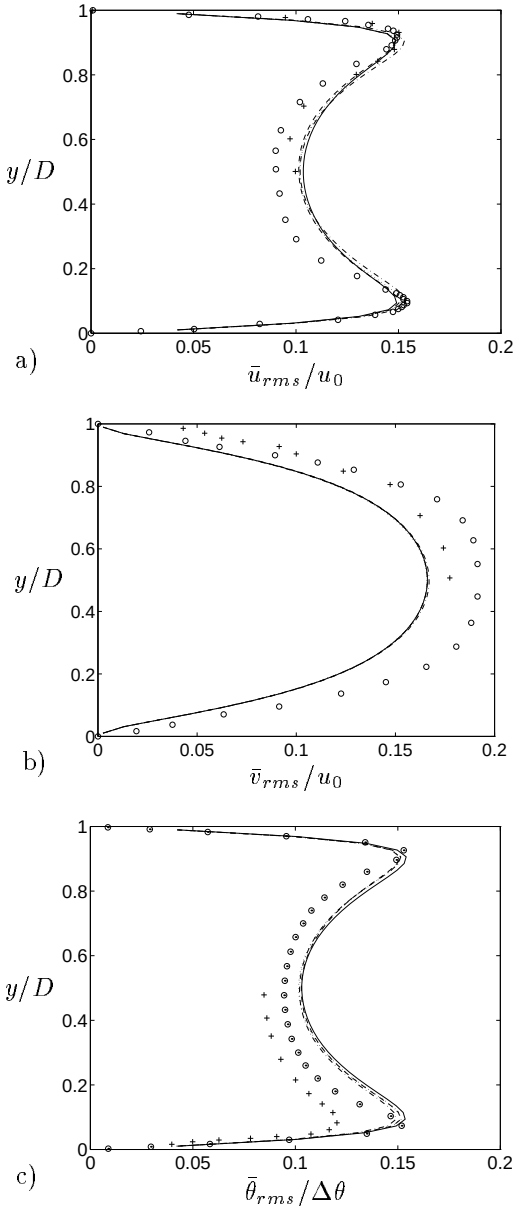

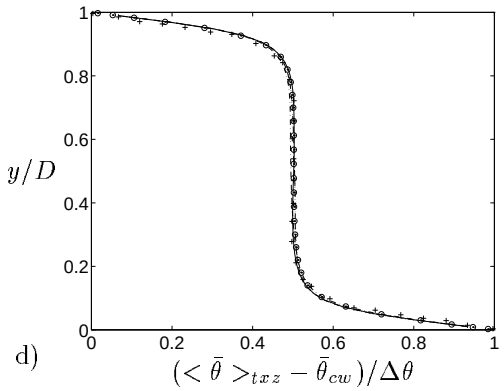

Figure 4: Vertical distributions of the root-mean-squares of the velocity components and temperature and the vertical profile for the dimensionless temperature: a) $\bar{u}_{rms}/u_0$; b) $\bar{v}_{rms}/u_0$; c) $\bar{\theta}_{rms}/\Delta\theta$; d) Dimensionless temperature, $(< \bar{\theta} >_{txz} - \bar{\theta}_{cw})/\Delta\theta$. Dotted line: Scalar model; Dashed line: Modified model ($Pr_t = 0.4$); Solid line: Modified model (Pr_t computed with Eq. (22)); Dash-dotted line: Buoyancy model ($Pr_t = 0.4$); + Experimental data from Ref. (29); ∘ DNS data ($Pr = 1.0$) from Ref. (27); ∘ DNS data ($Pr = 0.71$) from Ref. (28).

term hardly have any effects in the core region of the flow domain, where this term becomes nearly zero. The SGS eddy coefficients, ν_t and α_t, thus depend mainly on the strain term without being affected by Pr_t. In this region, both the modified model and the buoyancy model show behaviors similar to the scalar model. Within a range of $y/D \simeq 0.2$ near the wall, however, the buoyancy term plays an increasing role towards the wall surface in the determination of SGS eddy coefficients. Approaching the wall, both the strain and buoyancy terms increase, but their effects are actually suppressed to become insignificant owing to very small near-wall coefficients C and C_t (see Fig. 2).

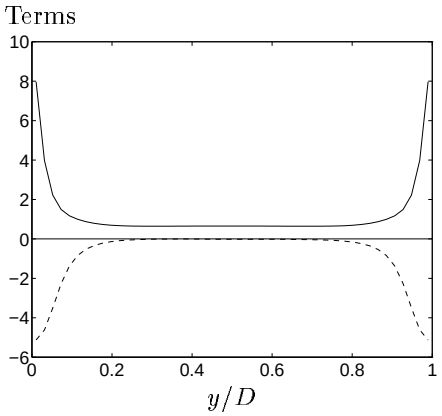

Figure 5: Comparison of the strain term, $\mid \bar{S} \mid^2$, and the buoyancy term, $\frac{g\beta}{Pr_t}\frac{\partial \bar{\theta}}{\partial y}$, using the modified base model with $Pr_t = 0.4$. Solid line: Strain term; Dashed line: Buoyancy term.

The SGS eddy coefficients computed with different models are further compared in Fig. 6. The

distributions in this figure correspond well to the profiles for the model coefficients in Fig. 2. The modified model gives the smallest model coefficients and thus the lowest SGS turbulence level. Very close to the wall ($y/D \simeq 0.06$), the models give negative Pr_t as shown in Fig. 3, owing to negative model coefficients C or C_t whereby backscatter is active. The near-wall buoyancy effect is then fed back into the SGS model with a positive value, as Pr_t is locally determined with either the buoyancy model or the modified model. This in turn should have decreased the SGS time scale and thus increased the SGS eddy viscosity/diffusivity. Nevertheless, it should be noted that, in the viscous boundary layer, coefficients C and C_t have been dynamically set to be very small, as shown in Fig. 2. Consequently, the eddy coefficients in this layer become negligibly small and rather insensitive to a certain range of variation in Pr_t (positive or negative). Although there exist certain differences in the eddy coefficients determined by different models, only slight variations are found in the results. One of the reasons is that the SGS turbulence level is relatively low in the flow considered with a maximum ν_t/ν of about 0.2. This suggests that the simulation for the SGS scales relies to a certain extent on the viscous effects.

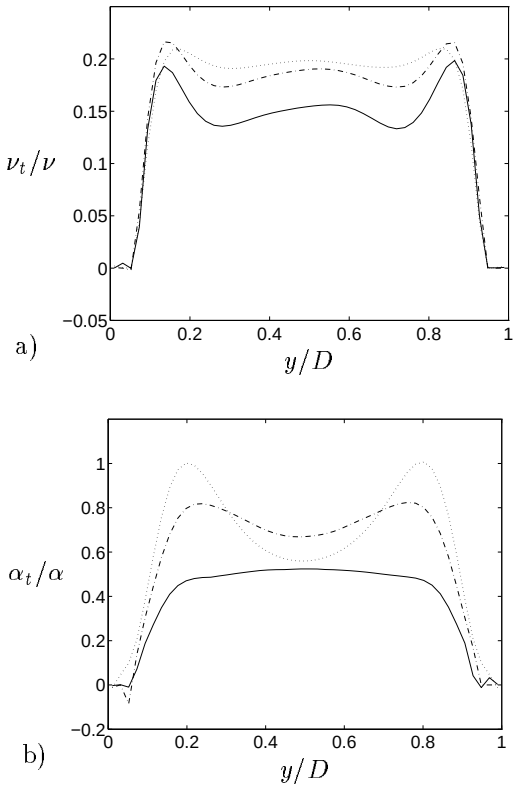

Figure 6: Comparison of SGS eddy coefficients, ν_t/ν and α_t/α: a) SGS eddy viscosity; b)SGS eddy diffusivity. Dotted line: Scalar model; Dash-dotted line: Buoyancy model (Pr_t computed with Eq. (22)); Solid line: Modified model (Pr_t computed with Eq. (22)).

Figure 7 presents the vertical profiles of the Nusselt number, Nu, computed with various models. The Nusselt number in this study is defined as

$$Nu = -\frac{< \bar{v}\bar{\theta} - \kappa \partial\bar{\theta}/\partial y >_{txz}}{\kappa \Delta\theta/D}. \qquad (27)$$

All the models give nearly identical simulations. The distribution of Nu is nearly uniform, with a value of about 6.4 within a wide core region. Near the walls, the Nusselt number varies owning to the large temperature gradient. For comparison, if the Nusselt number is redefined as $Nu = D|\ \partial\bar{\theta}/\partial y\ |_w/\Delta\theta$, the prediction given by the scalar model is 6.43, while it is 6.33 and 6.20, respectively, by the modified model and the buoyancy model with $Pr_t = 0.4$, and 6.29 and 6.08 when Pr_t is computed with equation (22). The measured value is 6.14 in air and 6.50 in gaseous helium (see Ref. (9) for experimental references).

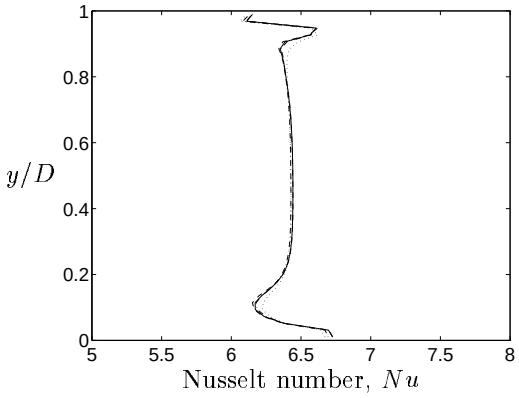

Figure 7: Vertical distribution of Nusselt number, Nu (same legend as in Fig. 4).

Figure 8 shows the vertical profiles for the vertical-velocity variance and skewness: $< v'^3 >_{txz}$ and $< v'^3 >_{txz}/< v'^2 >^{3/2}_{txz}$, where $v' = (\bar{v} - < \bar{v} >_t)$. Note that these quantities have been normalized with the velocity scale, u_0. The results show good agreement with the DNS data, even in the near-wall viscous layers where molecular diffusion and dissipation become dominant. The skewness is negative in the lower layer and positive in the upper layer. This result is consistent with the DNS data, and was well explained by Moeng and Rotunno (27) on deriving a relationship between the skewness and the ratio of updraft area and downdraft area. There is no apparent difference between the results computed with various models.

For a straightforward view of the flow structure, Figure 9 illustrates the vertical cross sections of the vertical velocity and temperature fluctuations. A few upward eddies are able to penetrate to the top. Some updrafts mix out their heat excess and are penetrated by downdrafts. As found in DNS (27), Fig. 9 indicates that the area occupied by an individual

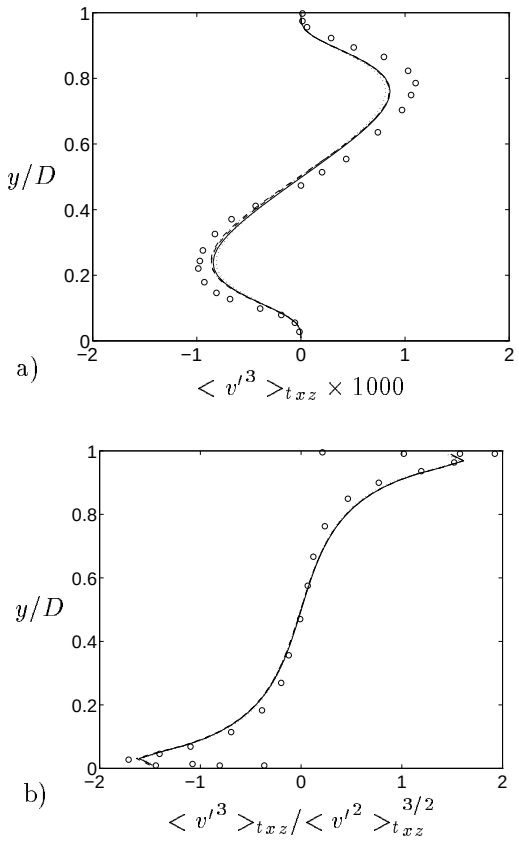

Figure 8: Vertical distributions of a) Variance of $\bar{v}$ and b) Skewness of $\bar{v}$ (same legend as in Fig. 4).

updraft remains nearly constant with height in the lower layers, although the vertical velocity increases over this lower portion. This phenomenon implies that the mass flux in the updraft is increased due to lateral entrainment in the lower layer. The temperature fluctuations correspond well to the vertical velocity contour. In general, the regions occupied by the thermals (with positive fluctuations) are those in which updrafts exist and *vice versa*.

Fig. 10 shows the horizontal cross sections of the vertical velocity and temperature fluctuations at three levels. Near the heated bottom wall, $y = 0.09$, small spots of downdrafts are surrounded by broad updrafts and *vice versa* near the cooled top wall ($y = 0.91$). This structure corresponds to the profile of the skewness of the vertical velocity $\bar{v}$ shown in Fig. 8. At the mid-level, $y = 0.51$, both the downdraft and the updraft penetrate with similar areas. The contour for the temperature fluctuations shows that the thermals near the heated bottom wall are narrow and elongated, while they are isolated near the cooled top wall. The eddy structure shown in this figure was also observed in DNS (27).

5 CONCLUDING REMARKS

Comparison have been made for three dynamic SGS models for handling turbulent convection flow with

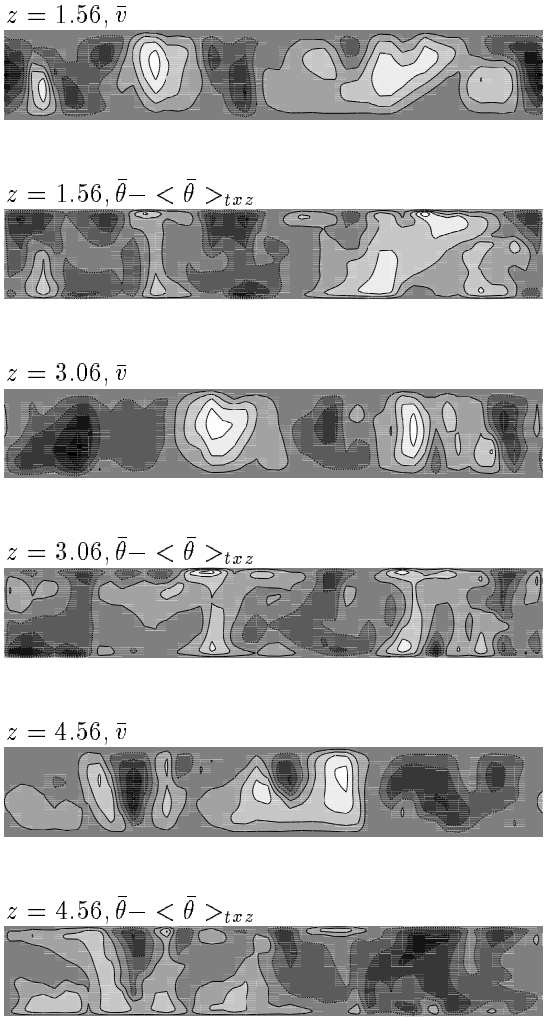

Figure 9: Instantaneous contours of $\bar{v}$ (contour interval is $0.1u_0$) and $\bar{\theta} - < \bar{\theta} >_{txz}$ (contour interval is $0.1\Delta\theta$) at vertical cross sections, simulated by the modified model using $Pr_t = 0.4$; the dark-colored areas indicate downdrafts and the light-colored areas indicate updrafts.

heat transfer. These include the scalar model, the buoyancy model and a modified buoyancy model. For thermally stratified flows, the buoyancy model may entail no-real solutions. To remedy this problem, the modified model re-constructs the time scaling in the SGS eddy viscosity/diffusivity formulation, and keeps the buoyancy effect being directly accommodated as in the buoyancy model. This model returns to the scalar model for isothermal flows. It thus works with fully developed turbulence generated by shear or by buoyancy, or by both. LES has been performed for the turbulent Rayleigh-Bénard flow at $Ra = 3.8 \times 10^5$ with these models. The results agree well with both the experimental and DNS data.

In comparison with the other models, the modified model gives very similar results for the flow considered. The model coefficients in various models, however, show rather different dynamic features. Corresponding with the computed smaller values of

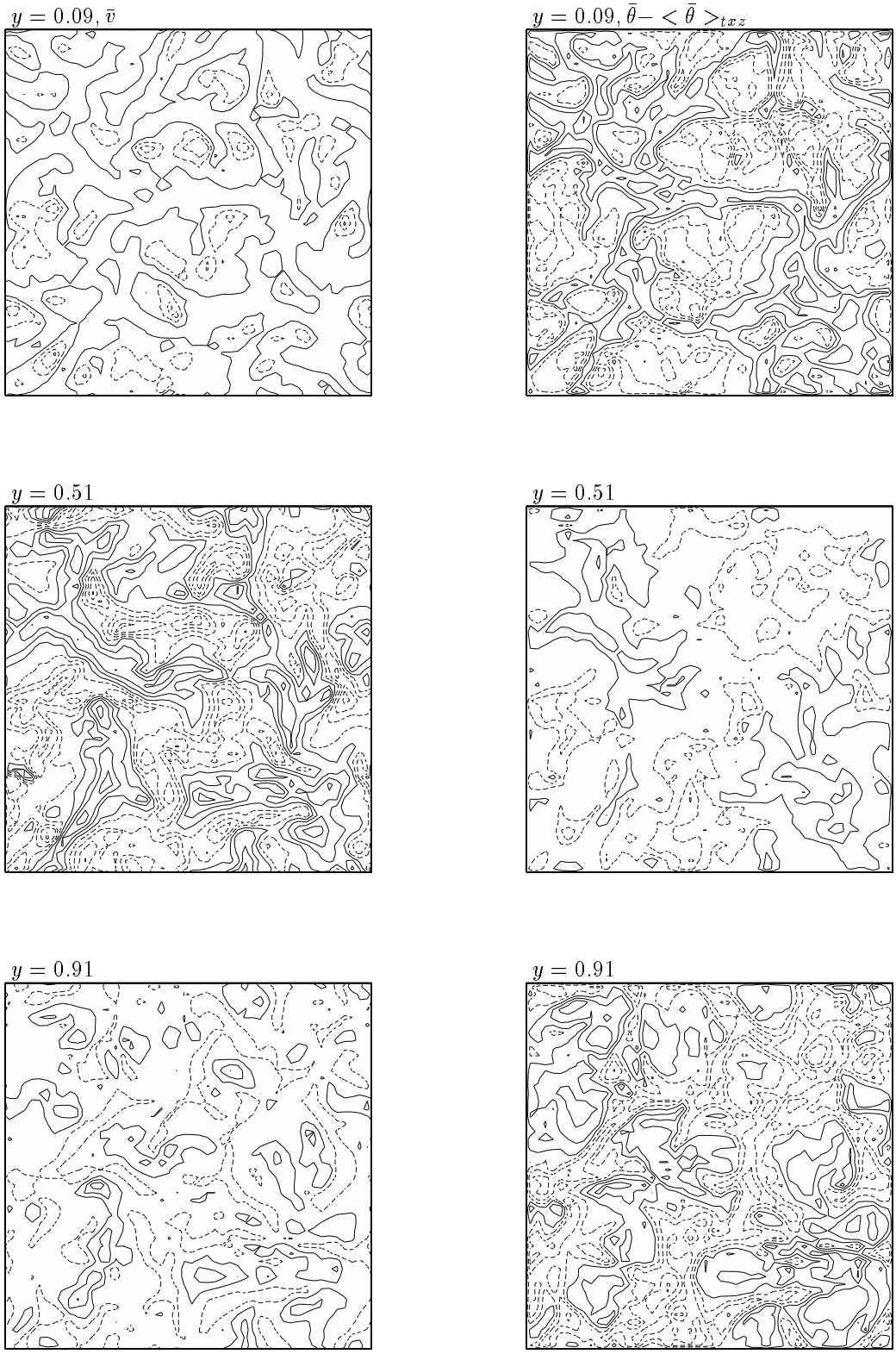

Figure 10: Instantaneous contours of $\bar{v}$ (contour interval is $0.1u_0$) and $\bar{\theta} - < \bar{\theta} >_{txz}$ (contour interval is $0.1\Delta\theta$) at horizontal cross sections, simulated by the modified model using $Pr_t = 0.4$; the solid and dotted contour lines indicate positive and negative values, respectively.

coefficients C and C_t, the modified model returns lower SGS eddy viscosities and diffusivities out of the near-wall boundary layer. However, only a small variation is found in the resultant simulations. This might be attributed to the relatively low turbulence level in the Rayleigh-Bénard convection flow considered. In future work, these SGS models need to be further investigated in applications to highly turbulent thermal convection flows.

REFERENCES

(1) Smagorinsky, J. General circulation experiments with the primitive equations, *Monthly Weather Review*, 1963, Vol. 91, pp. 99-165.

(2) Ferziger, J.H. Large eddy numerical simulations of turbulent flows, *AIAA J.*, 1977, Vol. 15, pp. 1261-1267.

(3) Bardina, J., Ferziger, J.H. and Reynolds, W.C. Improved subgrid scale models for large eddy simulation, AIAA Paper 80-1357, Snomass, Colorado, 1980.

(4) Yakhot, A., Orszag, S.A. and Yakhot, V. Renormalization group formulation of large eddy simulations, *J. Sci. Comp.*, 1989, Vol. 4, pp. 139-158.

(5) Moin, P., Squires, K., Cabot, W. and Lee, S. A dynamic subgrid-scale model for compressible turbulence and scalar transport, *Phys. Fluids A*, 1991, Vol. 11, pp. 2746-2757.

(6) Germano, M., Piomelli, U., Moin, P. and Cabot, W.H. A dynamic subgrid-scale eddy viscosity model, *Phys. Fluids A*, 1991, Vol. 3, pp. 1760-1765.

(7) Germano, M., Piomelli, U., Moin, P. and Cabot, W.H. Erratum, *Phys. Fluids A*, 1991, Vol. 3, pp. 3128.

(8) Piomelli, U., Cabot, W.H., Moin, P. and Lee, S. Subgrid-scale backscatter in turbulent and transitional flows, *Phys. Fluids A*, 1991, Vol. 3, pp. 1766-1771.

(9) Cabot, W. Large-eddy simulations of time-dependent and buoyancy-driven channel flows, in *Annual research Brief*, 1992, pp. 45-60, Center for Turbulence Research, Stanford Univ./NASA Ames Research Center.

(10) Eidson, T.M. Numerical simulation of the turbulent Rayleigh-Bénard problem using subgrid modelling, *J. Fluid Mech.*, 1985, Vol. 158, pp. 245-268.

(11) Wong, V.C. and Lilly, D.K. A comparison of two dynamic subgrid closure methods for turbulent thermal convection, *Phys. Fluids A*, 1994, Vol. 6, pp. 1016-1023.

(12) Bergstrom, D.J. and Huang, X. LES of buoyant cavity flow: Challenges for subgrid scale models, in *Proc. 2nd Int. Symp. on Turbulence, Heat and Mass Transfer*, 1997, pp. 421-430, Delft University Press.

(13) Wang, V.M. and Pletcher, R.H. On the large eddy simulation of a turbulent channel flow with significant heat transfer, *Phys. Fluids A*, 1996, Vol. 8, pp. 3354-3366.

(14) Canuto, V.M., Dubovikov, M.S. and Dienstfrey, A. A dynamic model for turbulence: IV. Buoyancy-driven flows, *Phys. Fluids A*, 1997, Vol. 9, pp. 2118-2131.

(15) Peng, S.-H. and Davidson, L. A proposed subgrid-scale model in large eddy simulation for turbulent thermal convection flow, Report 97/21, 1997, Department of Thermo and Fluid Dynamics, Chalmers University of Technology, Gothenburg.

(16) Cabot, W. and Moin, P. Large-eddy simulations of scalar transport with the dynamic subgrid-scale model, in *Large Eddy Simulation of Complex Engineering and Geophysical Flows*, 1993, pp. 141-158, Cambridge University Press, New York.

(17) Moin, P. A new approach for large eddy simulation of turbulence and scalar transport, in *Proc. Monte Veritá Coll. on Turbulence*, 1993, Birkhäuser, Bale.

(18) Winckelmans, G.S., Lund, T.S., Carati, D. and Wray, A.A. A priori testing of subgrid-scale models for the velocity-pressure and vorticity-velocity formulations, in *Proc. Summer Program*, 1996, pp. 309-328, Center for Turbulence Research, Stanford Univ./NASA Ames Research Center.

(19) Lilly, D.K. A proposed modification of the Germano subgrid-scale closure method, *Phys. Fluids A*, 1992, Vol. 4, pp. 633-635.

(20) Piomelli, U. and Liu, J. Large-eddy simulation of rotating channel flow using a localized dynamic model, *Phys. Fluids A*, 1995, Vol. 7, pp. 839-848.

(21) Sullivan, P.P. and Moeng, C.-H. An evaluation of the dynamic subgrid scale model in buoyancy-driven flows, in *Proc. 10th Symp. on Turbulence and Diffusion*, 1993, pp. 82-91, Portland, Oregon.

(22) Davidson, L. LES of recirculating flow without any homogeneous direction: A dynamic one-equation subgrid model, in *Proc. 2nd Int. Symp. on Turbulence, Heat and Mass Transfer*, 1997, pp. 481-490, Delft University Press.

(23) Davidson, L. and Farhanieh, B. CALC-BFC: A finite-volume code employing collocated variable arrangement and Cartesian velocity components for computation of fluid flow and heat transfer in complex three-dimensional geometries. Report 92/4, 1992, Department of Thermo and Fluid Dynamics,

Chalmers University of Technology, Gothenburg.

(24) Emvin, P. and Davidson, L. Development and implementation of a fast large eddy simulations method. Report, 1997, Department of Thermo and Fluid Dynamics, Chalmers University of Technology, Gothenburg.

(25) Zang, Y., Street, R.L. and Koseff, J.R. A dynamic mixed subgrid-scale model and its application to turbulent recirculating flows, *Phys. Fluids A*, 1993, Vol. 5, pp. 3186-3196.

(26) Davidson, L. Implementation of a large eddy simulation method applied to recirculating flow in a ventilated room. Report ISSN 1385-7956 R9611, 1996, Department of Building Technology and Structural Engineering, Aalborg University.

(27) Moeng, C.-H. and Rotunno, R. Vertical-velocity skewness in the buoyancy-driven boundary layer, *J. Atomos. Sci.*, 1990, Vol. 47, pp. 1149-1162.

(28) Wörner, M. and Grötzbach, G. DNS database of turbulent convection in horizontal fluid layers, in http://hbksun17.fzk.de:8080/IRS/eng/IRS3turbit_DNS_database.html.

(29) Deardorff, J.W. and Willis, G.E. Investigation of turbulent thermal convection between horizontal plates, *J. Fluid Mech.*, 1967, Vol. 28, pp. 675-704.